

Galactic absorption measured by X-ray observations of clusters of galaxies at the low Galactic latitude

Yumiko ANRAKU¹, Shigeo YAMAUCHI^{1,*}, Anje YOSHIMOTO¹, Masayoshi NOBUKAWA², Kumiko K. NOBUKAWA³, and Hideki UCHIYAMA⁴

¹Faculty of Science, Nara Women's University, Kitauoyanishimachi, Nara, Nara 630-8506, Japan

²Faculty of Education, Nara University of Education, Takabatake-cho, Nara, Nara 630-8528, Japan

³Faculty of Science and Engineering, Kindai University, 3-4-1 Kowakae, Higashi-Osaka 577-8502, Japan

⁴Faculty of Education, Shizuoka University, 836 Ohya, Suruga-ku, Shizuoka, Shizuoka 422-8529, Japan

*E-mail: yamauchi@cc.nara-wu.ac.jp

Abstract

The amount of the interstellar gas in the Galaxy has been conventionally estimated through observations at various wavelengths. The estimation of the total hydrogen column density (N_{H}) depends on assumptions such as temperature. The X-ray absorption process is the photoelectric absorption, which depends on the number of atoms to encounter X-ray photons, and hence X-ray observations would be able to derive the N_{H} values independently on the condition of the interstellar matter. We measured the Galactic absorption using clusters of galaxies at the low Galactic latitude. Comparing the observed N_{H} with the calculated N_{H} values from H I and CO intensities indicates that the observed values are systematically larger than the calculated values. The observed N_{H} values at high Galactic latitude ($N_{\text{H}} < 10^{22} \text{ cm}^{-2}$) are comparable to those estimated from $N_{\text{H I}}$ and optical reddening values using the method by Willingale et al. (2013, MNRAS, 431, 394), but the values near to the Galactic plane ($N_{\text{H}} > 10^{22} \text{ cm}^{-2}$) are larger than the estimated ones. The dust optical depth at 353 GHz, τ_{353} , and the observed N_{H} values are expressed by a linear function of $N_{\text{H}} = (1.01 - 1.59) \times 10^{26} \tau_{353} \text{ cm}^{-2}$ even at $N_{\text{H}} > 10^{23} \text{ cm}^{-2}$. We also confirmed a linear correlation between the optical reddening, $E(B - V)$, and the N_{H} values expressed by $N_{\text{H}} = (6.3 - 9.5) \times 10^{21} E(B - V) \text{ cm}^{-2}$. This work is an additional and independent test of the relation among the amount of interstellar gas, the optical depth, and the optical reddening.

Keywords: ISM: abundances — ISM: atoms — ISM: molecules — dust, extinction — X-rays: ISM

1 Introduction

The Galaxy consists of stars, star clusters, interstellar matter (ISM), cosmic rays, and so on. ISM in the Galaxy is composed of gas and dust. ISM have been measured by survey observations in various wavelengths (e.g., Dicky & Lockman 1990; Dame et al. 2001; Schlegel et al. 1998; Planck Collaboration 2011).

The amount of the interstellar gas in the Galaxy has been conventionally estimated by radio observations of atomic hydrogen (H I) and molecular hydrogen (H₂). The distribution of H I gas is observed by survey observations in the radio band at $\lambda=21$ cm (Dicky & Lockman 1990; Kalberla et al. 2005; HI4PI collaboration 2016). In the optically thin case, the H I column density ($N_{\text{H I}}$) is expressed as follows (Dicky & Lockman 1990),

$$N_{\text{H I}} = 1.823 \times 10^{18} \times W_{\text{H I}}, \quad (1)$$

where $W_{\text{H I}}$ is a velocity-integrated intensity of the H I emission at $\lambda=21$ cm.

The amount of H₂ is estimated from CO line surveys at $\lambda=2.6$ mm (e.g., Dame et al. 2001). The H₂ column density (N_{H_2}) is expressed as follows (Bolatto et al. 2013),

$$N_{\text{H}_2} = X_{\text{CO}} \times W_{\text{CO}}, \quad (2)$$

where X_{CO} is a conversion factor and W_{CO} is a velocity-integrated intensity of ¹²CO $J=1-0$. Based on the line observations in the radio band, the hydrogen column density, N_{H} , is usually estimated as a sum of the column densities of H I and H₂,

$$N_{\text{H}} = N_{\text{H I}} + 2N_{\text{H}_2}. \quad (3)$$

The amount of dust is usually measured from extinction, reddening, or thermal emission at sub-millimeter to infrared wavelengths. The relation between optical extinction, A_V , and N_{H} values has been observationally examined. Using two X-ray binaries together with the two extended sources, Reina & Tarengi (1973) derived the first linear relation by $N_{\text{H}} = 1.85 \times 10^{21} A_V \text{ cm}^{-2}$. Then, several authors measured the relation using various objects, $N_{\text{H}} = (1.79 - 2.22) \times 10^{21} A_V \text{ cm}^{-2}$ (Gorenstein 1975; Predehl & Schmitt 1995; Güver & Özel 2009). Recently, Gatuzz et al. (2024) reported the best-fit relation by $N_{\text{H}} = (4.82 \pm 0.08) \times 10^{21} A_V + (0.59 \pm 0.16) \times 10^{21} \text{ cm}^{-2}$ using coronal sources observed during the initial eROSITA all-sky survey. The relation between optical reddening, $E(B - V)$, and N_{H} values has also been examined. The relation was expressed by $N_{\text{H}} = 5.8 \times 10^{21} E(B - V) \text{ cm}^{-2}$ (e.g., Bohlin et al. 1978) and recent studies proposed $N_{\text{H}} = (7.7 - 9.4) \times 10^{21} E(B - V) \text{ cm}^{-2}$ (e.g., Hensley & Draine 2017; Lenz et al. 2017; Li et al. 2018).

By comparing distributions of Gamma-rays and interstellar gas measured with H I and CO surveys, the amount of gas estimated from the Gamma-rays is larger than that estimated from H I and CO lines. Based on the results, a hypothesis that a considerable amount of gas is not properly traced by H I or CO surveys is proposed, called a dark gas scenario (Grenier et al. 2005). Planck observations have provided high-quality all-sky data at submillimeter wavelengths, including whole-sky distributions of dust op-

tical depth at 353 GHz (τ_{353}) and dust temperature (T_d) (Planck Collaboration 2014; Planck Collaboration 2016) and the dark gas was also suggested (Planck Collaboration 2011). To explain the features, two hypotheses have been proposed, CO-dark H₂ gas (e.g., Wolfire et al. 2010; Smith et al. 2014) and optically thick H I gas (e.g., Fukui et al. 2014, 2015). Based on the good correlation between gas and dust distributions (e.g., Bohlin et al. 1978), the total N_H value of ISM can be estimated from dust properties. Assuming a constant gas-to-dust ratio and uniform dust properties, Fukui et al. (2014, 2015) examined a relationship between the N_{H1} value and τ_{353} . They suggested that a relationship for the optically thin H I gas is good, but W_{H1} does not follow τ_{353} for the optically thick case: W_{CO} is saturated in the high density case on the Galactic plane. Thus, it is difficult to accurately assess the total N_H value from H I and CO surveys in high-density regions.

X-rays coming along lines of sight through the Galaxy is suffered from the photoelectric absorption by the ISM, but in the hard X-ray band, the interstellar medium is transparent even for the line of sight through the Galactic plane. Therefore, X-ray observation for extragalactic objects in the wide energy band, such as 1–10 keV, is a powerful tool to measure the N_H value in the Galaxy.

Using X-ray afterglows of gamma-ray bursts, energetic phenomena occurred in external galaxies, Willingale et al. (2013) investigated the total N_H value in the direction of the gamma-ray bursts. They derived a simple function for the N_{H_2} value composed of N_{H1} and $E(B - V)$ as follows,

$$N_{H_2} = N_{H_2\max} [1 - \exp(-\frac{N_{H1}E(B - V)}{N_c})], \quad (4)$$

where $N_{H_2\max}$ and N_c are constants to be derived from the fitting. Combining the N_{H1} value, they concluded that the empirical function represents a significant revision in Galactic absorption compared to the previous standard methods, particularly at low Galactic latitudes. However, two issues are considered. First, the estimation has uncertainty due to intrinsic absorption by the host galaxies where the Gamma-ray burst sources exist. Second, objects on the Galactic plane with a large N_H value ($>10^{22}$ cm⁻²) are limited in their sample. Thus, a method to estimate the total N_H value on the Galactic plane of $b \sim 0^\circ$ ($N_H > 10^{22}$ cm⁻²) has not yet been accurately established.

Clusters of galaxies are bright X-ray sources with a luminosity of 10^{40} – 10^{46} erg s⁻¹ in the X-ray band (e.g., Fukazawa et al. 2004). X-rays from clusters of galaxies originate from a hot plasma gas with a temperature of ~ 0.5 –10 keV and hence their spectra are simply expressed by a redshifted thin thermal plasma model. Since clusters of galaxies have no intrinsic absorption, they are more suitable target for investigating N_H of ISM than afterglows of gamma-ray bursts. Although the number of clusters of galaxies located near to the Galactic plane is limited, X-ray observations have discovered several candidates in the direction of low Galactic latitude (e.g., Nevalainen et al. 2001; Lopes de Oliveira et al. 2006; Yamauchi et al. 2010; Yamauchi et al. 2011; Mori et al. 2013; Barrière et al. 2015; Nobukawa et al. 2015; Yamauchi & Ueno 2025). Some of them are located at $b \sim 0^\circ$ and have large N_H values of 10^{22} – 10^{23} cm⁻². Thus, these are good samples to evaluate the amount of the ISM along the line of sight in the Galaxy.

Based on the idea, we selected 17 spectral data of 16 clusters of galaxies and candidates located at the low Galactic latitude whose results have been published, and carried out reanalysis of the data. We compared the observed N_H values with values estimated from equation (3) and the method using equation (4) (Willingale et al. 2013). In addition, we also examined a relationship among the observed N_H value, τ_{353} , $E(B - V)$ values, and confirmed that

they are well correlated even at $N_H > 10^{23}$ cm⁻². In this paper, we represent the results of the spectral analysis and the relationship.

2 X-ray data

We utilized the ASCA, Suzaku, and XMM-Newton archival data. The ASCA and Suzaku data were provided by DARTS/JAXA, whereas the XMM-Newton data were provided by XMM-Newton Science Archive/ESA.

The ASCA observations were carried out with the two Solid-state Imaging Spectrometers (SIS0, SIS1: Burke et al. 1991) and the two Gas Imaging Spectrometers (GIS2, GIS3: Makishima et al. 1996; Ohashi et al. 1996) placed at the focal plane of the thin foil X-ray Telescope (XRT: Serlemitsos et al. 1995). Since the GIS had a large field of view to cover the whole target, we utilized the GIS data. The GIS was operated in PH mode. We analyzed data of a cluster of galaxies and a candidate, 3C129.1 and AX J145732–5901.

The Suzaku data were obtained from the X-ray Imaging Spectrometer (XIS: Koyama et al. 2007) placed at the focal planes of the thin foil X-ray Telescopes (XRT: Serlemitsos et al. 2007). The XIS was operated in the normal clocking mode. We analyzed 11 spectral data of 10 clusters of galaxies and candidates, AX J185905+0333, Suzaku J1840.2–0544, CIZA 2242.8+5301, Suzaku J1759–3450, Cygnus A Cluster, 2XMM J045637.2+522411, CIZA J1700.84–3144, A3627, Ophiuchus Cluster, northwest (NW) and southeast (SE) regions of CIZA J1358.9–4750.

The XMM-Newton data were obtained with the European Photon Imaging Camera (EPIC). The EPIC system is composed of two different detectors; two MOS cameras (MOS 1 and MOS 2: Turner et al. 2001) and one pn camera (Strüder et al. 2001). The MOS and pn cameras were operated in the full-frame mode. We analyzed data of 4 clusters of galaxies and candidates, XMMU J183225.4–103645, IGR J17448–3232, CIZA J1324.7–5736, and CI 2334+48. The logs of the ASCA, Suzaku, and XMM-Newton observations are listed in table 1.

3 Analysis and results

3.1 Spectral analysis

We conducted spectral analysis for ASCA, Suzaku, and XMM-Newton data. The ASCA and Suzaku data analysis was performed using the HEASoft, whereas the XMM-Newton data analysis was performed using the Extended Source Analysis Software (ESAS) package and the HEASoft.

A source spectrum was extracted from a source region centered on the X-ray emission, whereas a background spectrum was estimated from nearby blank sky data. According to Snowden et al. (2008), for the XMM-Newton data, we took account of soft proton contamination (a time-variable flare component and a quiescent continuum component) and instrumental fluorescence lines for the non-X-ray background.

The source spectrum after excluding the sky and non-X-ray background components was fitted with a thin thermal plasma model (apec in XSPEC, Smith et al. 2001) modified by photoelectric absorption. The atomic data of the lines and continua of the thin thermal plasma were taken from ATOMDB 3.0.9. For the abundance table, several data are available. Here, we utilized three abundance tables from Anders & Grevesse (1989) (hereafter angr), Lodders (2003) (hereafter lodd), and Wilms et al. (2000)

Table 1. Observation logs.

Target name Observation ID	Obs. position RA, Dec (J2000.0) <i>l, b</i>	Start time End time	Exposure (ks)	Note*
ASCA				
AX J145732–5901	14 ^h 58 ^m 30 ^s .61, –58°55′32″.0	1999-02-23 23:40:34	11.2	1
57004070	318°700, –0°000	1999-02-24 10:30:41		
3C129.1	4 ^h 49 ^m 35 ^s .47, +45°06′43″.0	1998-08-31 01:34:41	44.1	2
86050000	160°400, +0°266	1998-09-01 12:10:41		
Suzaku				
AX J185905+0333	18 ^h 59 ^m 12 ^s .22, +3°34′52″.7	2010-04-17 17:35:13	51.0	3
505027010	37°004, –0°092	2010-04-18 21:09:18		
Suzaku J1840.2–0544	18 ^h 40 ^m 35 ^s .30, –5°36′32″.4	2011-03-27 15:21:16	49.6	4
505090010	26°705, –0°152	2011-03-28 19:00:18		
CIZA J2242.8+5301	22 ^h 43 ^m 02 ^s .45, +53°09′41″.8	2011-07-28 13:19:44	122.9	5
806001010	104°280, –4°996	2011-07-30 19:42:16		
Suzaku J1759–3450	17 ^h 59 ^m 10 ^s .13, –34°49′09″.8	2012-03-07 21:40:15	40.2	6
406019010	356°383, –5°461	2012-03-08 21:54:13		
Cygnus A Cluster	19 ^h 59 ^m 02 ^s .62, +40°47′18″.6	2008-11-15 21:43:08	44.7	7
803050010	76°195, +5°853	2008-11-16 21:58:19		
2XMM J045637.2+522411	04 ^h 56 ^m 53 ^s .52, +52°25′02″.6	2007-02-16 15:40:27	50.5	8
501075010	155°484, +5°809	2007-02-17 18:08:24		
CIZA J1700.84–3144	17 ^h 00 ^m 47 ^s .04, –31°44′42″.7	2013-02-18 11:50:13	8.9	9
407027010	352°212, +6°400	2013-02-18 18:00:11		
A3627	16 ^h 14 ^m 16 ^s .13, –60°50′59″.6	2009-03-15 22:09:21	46.0	10
803032010	325°259, –7°106	2009-03-16 14:34:24		
Ophiuchus Cluster	17 ^h 12 ^m 26 ^s .23, –23°22′44″.4	2007-09-24 21:12:15	100.5	11
802046010	0°562, +9°269	2007-09-27 14:15:16		
CIZA J1358.9–4750	13 ^h 58 ^m 36 ^s .24, –47°46′32″.9	2013-01-21 18:07:12	61.7	12
807037010	314°453, +13°588	2013-01-23 11:36:20		
XMM-Newton				
XMMU J183225.4–103645	18 ^h 32 ^m 51 ^s .97, –10°35′47″.0	2000-04-11 12:26:55	34.2	13
0122700301	21°397, –0°747	2000-04-11 21:57:00		
IGR J17448–3232	17 ^h 44 ^m 53 ^s .41, –32°32′54″.0	2012-02-26 04:16:42	43.9	14
0672260101	356°836, –1°750	2012-02-26 16:28:41		
CIZA J1324.7–5736	13 ^h 24 ^m 47 ^s .02, –57°36′34″.0	2003-08-16 20:49:50	12.2	15
0152131201	307°403, +4°973	2003-08-17 00:13:58		
CI 2334+48	23 ^h 33 ^m 39 ^s .96, +48°49′05″.9	2001-01-28 15:00:38	25.2	16
0093552701	109°979, –12°088	2001-01-28 22:01:00		

* Previous works. 1: Yamauchi & Ueno (2025), 2: Taylor et al. (2001), 3: Yamauchi et al. (2011), 4: Nobukawa et al. (2015), 5: Akamatsu & Kawahara (2013), 6: Mori et al. (2013), 7: Smith et al. (2002), 8: Yamauchi et al. (2010), 9: Mori et al. (2017), 10: Nishino et al. (2022), 11: Fujita et al. (2008), 12: Kato et al. (2015), 13: Nevalainen et al. (2001), 14: Barrière et al. (2015), 15: Mullis et al. (2005), 16: Lopes de Oliveira et al. (2006).

(hereafter `wilm`). For the model of the photoelectric absorption, we utilized a `phabs` model with the cross-sections of the photoelectric absorption taken from Verner et al. (1996). In this analysis, we assumed the abundances of ISM to be solar. Thus, we applied the spectral model as follows,

Model 1 (`phabs, angr`): `phabs`×`apec` (`angr`)

Model 2 (`phabs, lodd`): `phabs`×`apec` (`lodd`)

Model 3 (`phabs, wilm`): `phabs`×`apec` (`wilm`)

To examine the difference in the cross sections of low-energy absorption, we utilized another absorption model, `tbabs` (Wilms et al. 2000) which calculates the cross sections for X-ray absorption due to the gas-phase ISM, the grain-phase ISM, and the molecules in the ISM. The applied spectral model is as follows,

Model 4 (`tbabs, wilm`): `tbabs`×`apec` (`wilm`)

Free parameters are normalization, electron temperature, red-

shift, and abundance of the plasma gas in clusters of galaxies, and the N_{H} value of photoelectric absorption. The best-fitting results are listed in tables 2-4 for each target. We note that the results are basically consistent with those in the previous works listed in tables 2-4.

Comparing the results obtained using three abundance tables, we found that the N_{H} values using `lodd` and `wilm` are consistent with each other, but that using `angr` is systematically smaller than the others. On the other hand, the results using the `phabs` model (model 3) and the `tbabs` model (model 4) are almost the same.

3.2 N_{H} values estimated from the previous methods

Using the results derived from radio band observations, we estimate the Galactic N_{H_1} and N_{H_2} column densities of the line of sight toward clusters of galaxies and then evaluate the total N_{H}

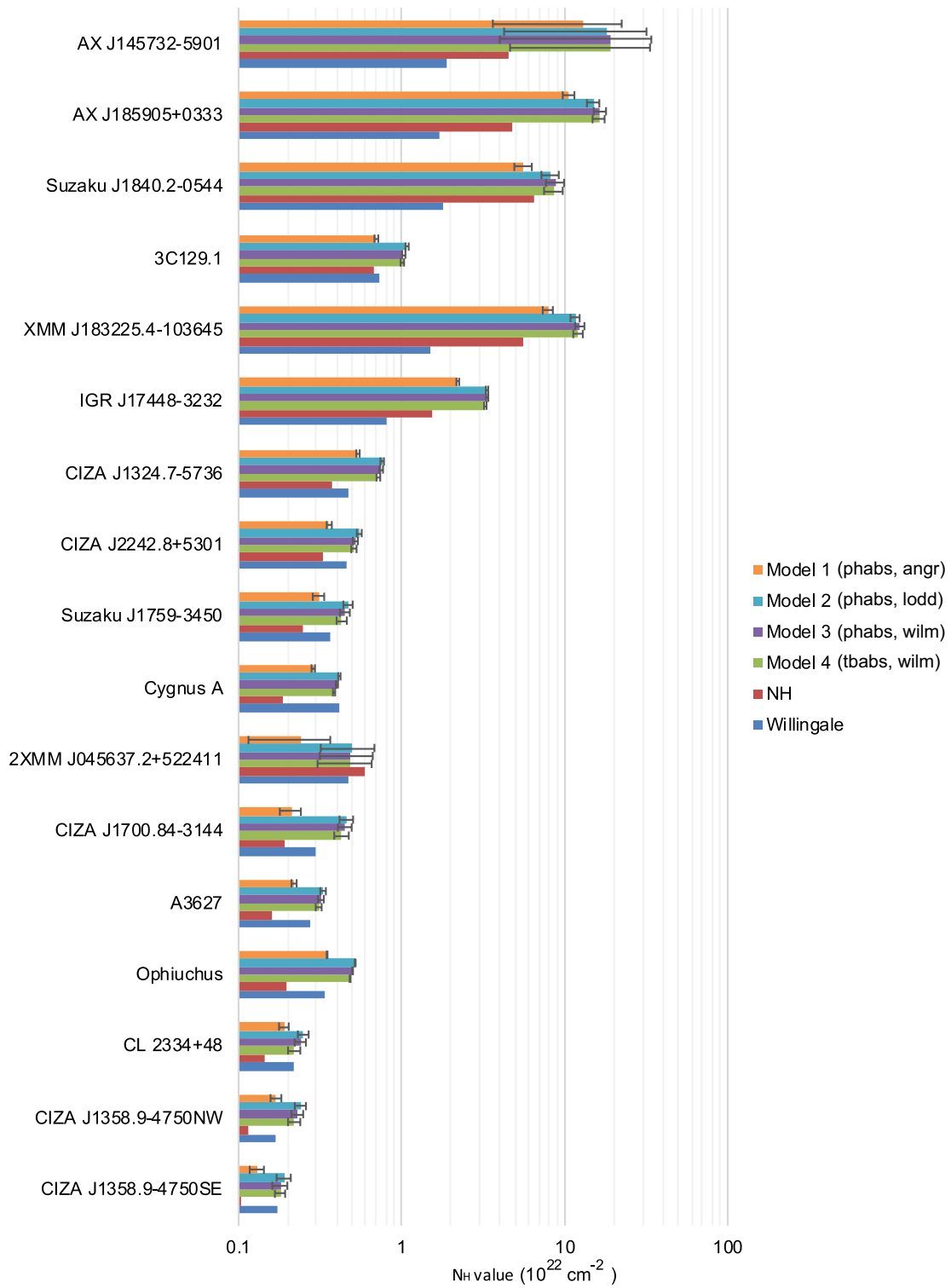


Fig. 1. Comparison of the observed N_{H} value with those estimated from the previous methods. Model 1–4: observed N_{H} values with an error of 68% confidence level, NH: N_{H} values estimated by equation (3), and Willingale: N_{H} values estimated by the method in Willingale et al. (2013). Alt text: A bar chart showing the best-fitting results.

Table 2. Best-fitting parameters for each target.

Parameter	Model 1 (phabs, angr)	Model 2 (phabs, lodd)	Model 3 (phabs, wilm)	Model 4 (tbabs, wilm)
AX J145732–5901				
N_{H} (10^{22} cm $^{-2}$)	13^{+15}_{-7}	18^{+22}_{-9}	19^{+24}_{-10}	19^{+23}_{-10}
kT_e (keV)	$2.6^{+4.9}_{-1.5}$	$2.6^{+4.6}_{-1.5}$	$2.7^{+4.8}_{-1.5}$	$2.7^{+4.8}_{-1.5}$
Abundance (Solar)	>0.36	>0.52	>0.63	>0.64
Redshift	0.12 ± 0.04	0.12 ± 0.04	0.12 ± 0.04	0.13 ± 0.04
Normalization* (10^{-3} cm $^{-5}$)	$8.2^{+67.0}_{-6.4}$	$8.6^{+74.5}_{-6.7}$	$7.5^{+66.9}_{-5.7}$	$7.7^{+66.3}_{-7.0}$
$\chi^2/\text{d.o.f.}$	27.5/31	27.8/31	27.7/31	27.7/31
AX J185905+0333				
N_{H} (10^{22} cm $^{-2}$)	10.6 ± 1.4	$15.0^{+2.1}_{-1.6}$	$16.5^{+2.3}_{-1.8}$	$16.2^{+2.2}_{-1.8}$
kT_e (keV)	5.8 ± 1.1	5.7 ± 1.1	5.8 ± 1.1	5.8 ± 1.1
Abundance (Solar)	0.32 ± 0.12	0.47 ± 0.18	$0.55^{+0.21}_{-0.16}$	$0.55^{+0.22}_{-0.16}$
Redshift	0.393 ± 0.006	0.393 ± 0.006	0.393 ± 0.006	0.393 ± 0.006
Normalization* (10^{-3} cm $^{-5}$)	5.6 ± 1.9	6.2 ± 2.2	5.6 ± 2.0	5.6 ± 2.0
$\chi^2/\text{d.o.f.}$	116.8/136	116.0/136	116.6/136	116.6/136
Suzaku J1840.2–0544				
N_{H} (10^{22} cm $^{-2}$)	5.6 ± 1.1	8.2 ± 1.6	8.8 ± 1.8	8.6 ± 1.8
kT_e (keV)	6.2 ± 1.5	6.1 ± 1.5	6.2 ± 1.4	6.2 ± 1.5
Abundance (Solar)	$0.61^{+0.23}_{-0.18}$	0.9 ± 0.4	1.0 ± 0.4	1.0 ± 0.4
Redshift	0.093 ± 0.007	0.093 ± 0.007	0.093 ± 0.007	0.093 ± 0.007
Normalization* (10^{-3} cm $^{-5}$)	2.3 ± 0.6	2.5 ± 0.7	2.3 ± 0.7	2.3 ± 0.7
$\chi^2/\text{d.o.f.}$	112.9/104	112.4/104	113.0/104	113.1/104
3C129.1				
N_{H} (10^{22} cm $^{-2}$)	0.70 ± 0.03	1.08 ± 0.04	1.03 ± 0.04	1.01 ± 0.04
kT_e (keV)	6.4 ± 0.3	6.2 ± 0.4	6.5 ± 0.3	6.5 ± 0.3
Abundance (Solar)	0.34 ± 0.04	0.51 ± 0.06	0.59 ± 0.07	0.59 ± 0.07
Redshift	$0.029^{+0.002}_{-0.009}$	0.025 ± 0.007	$0.029^{+0.002}_{-0.009}$	$0.028^{+0.003}_{-0.008}$
Normalization* (10^{-3} cm $^{-5}$)	76 ± 2	81 ± 2	75 ± 2	75 ± 2
$\chi^2/\text{d.o.f.}$	783.7/656	784.6/656	781.0/656	780.8/656
XMMU J183225.4–103645				
N_{H} (10^{22} cm $^{-2}$)	7.9 ± 0.9	11.6 ± 1.2	12.4 ± 1.3	12.1 ± 1.3
kT_e (keV)	5.6 ± 1.1	5.4 ± 1.1	5.6 ± 1.1	5.6 ± 1.1
Abundance (Solar)	0.60 ± 0.18	0.85 ± 0.25	1.03 ± 0.31	1.03 ± 0.31
Redshift	0.125 ± 0.004	0.125 ± 0.005	0.125 ± 0.004	0.125 ± 0.004
Normalization* (10^{-3} cm $^{-5}$)	2.6 ± 0.6	2.9 ± 0.7	2.6 ± 0.6	2.6 ± 0.6
$\chi^2/\text{d.o.f.}$	122.1/115	121.6/115	122.4/115	122.4/115
IGR J17448–3232				
N_{H} (10^{22} cm $^{-2}$)	2.21 ± 0.07	3.34 ± 0.09	3.35 ± 0.08	3.26 ± 0.09
kT_e (keV)	11.1 ± 0.9	10.3 ± 0.7	11.6 ± 1.0	11.6 ± 1.0
Abundance (Solar)	0.31 ± 0.04	0.44 ± 0.05	0.57 ± 0.07	0.57 ± 0.07
Redshift	0.054 ± 0.002	0.054 ± 0.002	0.054 ± 0.003	0.054 ± 0.003
Normalization* (10^{-3} cm $^{-5}$)	29.1 ± 0.6	32.0 ± 0.7	28.6 ± 0.5	28.5 ± 0.5
$\chi^2/\text{d.o.f.}$	1405.5/1496	1377.3/1496	1427.4/1496	1429.3/1496

Errors are provided at 90% confidence level.

* Defined as $10^{-14} \times \int n_{\text{H}} n_{\text{e}} dV / [4\pi D_{\text{A}}^2 (1+z)^2]$, where n_{H} is the hydrogen density (cm $^{-3}$), n_{e} is the electron density (cm $^{-3}$), D_{A} is the angular distance (cm), z is the redshift, and V is the volume (cm 3).

values by the equation (3). The N_{H_1} value was taken from the data in the HI4PI survey (HI4PI collaboration 2016). The pixel size of the data is $0^{\circ}083$. Using web tool¹, we estimated a weighted mean value within a cone radius of $0^{\circ}1$. The CO intensity, W_{CO} , at the target position was taken from data in Dame et al. (2001). The pixel size is $0^{\circ}125$. We utilized a value in the pixel including the target position. To convert W_{CO} to N_{H_2} value, we assumed $X_{\text{CO}}=1.8 \times 10^{20}$ cm $^{-2}$ K $^{-1}$ km $^{-1}$ s (Dame et al. 2001). Then, we

obtained the total N_{H} value from the equation (3). We also calculated the N_{H} value for the target position using the method in Willingale et al. (2013)².

Figure 1 displays comparisons of the observed N_{H} value listed in tables 2–4 and the calculated values using the previous methods. In all cases, the observed N_{H} values are larger than those calculated by equation (3). On the other hand, the values by the Willingale method are comparable to those of CGs at high Galactic

¹ <https://heasarc.gsfc.nasa.gov/cgi-bin/Tools/w3nh/w3nh.pl>

² <https://www.swift.ac.uk/analysis/nhtot/index.php>

Table 3. Best-fitting parameters for each target.

Parameter	Model 1 (phabs, angr)	Model 2 (phabs, lodd)	Model 3 (phabs, wilm)	Model 4 (tbabs, wilm)
CIZA J1324.7–5736				
N_{H} (10^{22} cm $^{-2}$)	0.54±0.02	0.76±0.03	0.75±0.03	0.72±0.03
kT_{e} (keV)	2.42±0.06	2.47±0.07	2.47±0.07	2.49±0.07
Abundance (Solar)	0.61±0.06	0.88±0.10	1.04±0.11	1.03±0.11
Redshift	0.019±0.002	0.019±0.004	0.019±0.002	0.019±0.002
Normalization* (10^{-3} cm $^{-5}$)	13.6±0.6	13.6±0.6	13.1±0.6	13.0±0.6
$\chi^2/\text{d.o.f.}$	1016.2/1047	997.8/1047	1009.1/1047	1007.5/1047
CIZA J2242.8+5301				
N_{H} (10^{22} cm $^{-2}$)	0.36±0.02	0.55±0.03	0.52±0.03	0.51±0.03
kT_{e} (keV)	7.4±0.5	7.4±0.5	7.5±0.5	7.6±0.5
Abundance (Solar)	0.22±0.05	0.33±0.07	0.39±0.08	0.39±0.08
Redshift	0.190±0.005	0.190±0.006	0.190±0.006	0.190±0.006
Normalization* (10^{-3} cm $^{-5}$)	3.71±0.10	3.91±0.11	3.65±0.10	3.64±0.10
$\chi^2/\text{d.o.f.}$	274.0/262	271.1/262	274.7/262	275.0/262
Suzaku J1759–3450				
N_{H} (10^{22} cm $^{-2}$)	0.31±0.04	0.47±0.05	0.45±0.05	0.43±0.05
kT_{e} (keV)	5.0±0.4	5.0±0.4	5.0±0.4	5.0±0.4
Abundance (Solar)	0.15±0.05	0.23±0.08	0.27±0.09	0.27±0.09
Redshift	0.130±0.007	0.130±0.007	0.130±0.007	0.130±0.007
Normalization* (10^{-3} cm $^{-5}$)	4.6±0.2	4.8±0.3	4.5±0.2	4.5±0.2
$\chi^2/\text{d.o.f.}$	195.7/172	195.1/172	196.2/172	196.7/172
Cygnus A Cluster				
N_{H} (10^{22} cm $^{-2}$)	0.287±0.011	0.415±0.011	0.401±0.010	0.385±0.010
kT_{e} (keV)	5.5±0.4	5.8±0.3	5.8±0.3	5.9±0.3
Abundance (Solar)	0.49±0.04	0.75±0.05	0.89±0.05	0.89±0.06
Redshift	0.058±0.001	0.058±0.001	0.058±0.001	0.058±0.001
Normalization* (10^{-3} cm $^{-5}$)	38.5±0.7	39.9±0.5	37.6±0.5	37.4±0.5
$\chi^2/\text{d.o.f.}$	2658.9/2502	2651.1/2502	2661.2/2502	2668.0/2502
2XMM J045637.2+522411				
N_{H} (10^{22} cm $^{-2}$)	0.34±0.20	0.50±0.29	0.49±0.28	0.48±0.28
kT_{e} (keV)	3.8±1.0	3.9±1.0	3.9±1.0	3.8±1.0
Abundance (Solar)	0.27±0.22	0.40±0.32	0.50±0.38	0.49±0.39
Redshift	0.162±0.016	0.163±0.017	0.163±0.016	0.161±0.016
Normalization* (10^{-3} cm $^{-5}$)	0.70±0.16	0.72±0.16	0.68±0.15	0.68±0.15
$\chi^2/\text{d.o.f.}$	92.5/105	93.2/105	92.3/105	92.3/105
CIZA J1700.84–3144				
N_{H} (10^{22} cm $^{-2}$)	0.31±0.05	0.46±0.07	0.45±0.07	0.43±0.07
kT_{e} (keV)	5.4±0.7	5.4±0.7	5.5±0.7	5.5±0.7
Abundance (Solar)	0.29 $^{+0.10}_{-0.05}$	0.44±0.14	0.51±0.17	0.51±0.16
Redshift	0.136±0.008	0.136±0.008	0.137±0.008	0.137±0.008
Normalization* (10^{-3} cm $^{-5}$)	6.5±0.4	6.8±0.5	6.4±0.4	6.4±0.4
$\chi^2/\text{d.o.f.}$	177.9/169	178.7/169	179.3/169	180.2/169

Errors are provided at 90% confidence level.

* Defined as $10^{-14} \times \int n_{\text{H}} n_{\text{e}} dV / [4\pi D_{\text{A}}^2 (1+z)^2]$, where n_{H} is the hydrogen density (cm $^{-3}$), n_{e} is the electron density (cm $^{-3}$), D_{A} is the angular distance (cm), z is the redshift, and V is the volume (cm 3).

latitude ($|b| \gtrsim 5^\circ$), suggesting that the estimation seems to be good, but they are smaller than those of 6 CGs with $N_{\text{H}} \gtrsim 10^{22}$ cm $^{-2}$ located near to the Galactic plane ($|b| < 2^\circ$).

3.3 Correlation between the N_{H} values and τ_{353}

The optical depth at 353 GHz, τ_{353} , is much less than 1, and hence the values of τ_{353} can trace the amount of matter along the line of sight. Using τ_{353} from the Planck all-sky data³, we examined a

correlation between the τ_{353} and the N_{H} values. The pixel size of the τ_{353} data is 1'. We used a mean τ_{353} value of 3×3 pixels centered on the pixel including the target position. Figure 2 shows a correlation plot between the τ_{353} and the N_{H} values derived from Model 1–4. All the models show that the observed N_{H} values well correlates with the τ_{353} values. The correlation coefficients are calculated to be 0.94–0.95.

We fitted the data with a linear relation using the Markov chain Monte Carlo (MCMC) method implemented in the Python package `emcee` (Foreman-Mackey et al. 2013). The measurement uncertainties were taken into account, and the intrinsic scatter was

³ http://irsa.ipac.caltech.edu/data/Planck/release_1/all-sky-maps/

Table 4. Best-fitting parameters for each target.

Parameter	Model 1 (phabs, angr)	Model 2 (phabs, lodd)	Model 3 (phabs, wilms)	Model 4 (tbabs, wilms)
A3627				
N_{H} (10^{22} cm $^{-2}$)	0.219±0.012	0.33±0.02	0.32±0.02	0.31±0.02
kT_e (keV)	6.0±0.2	6.1±0.2	6.1±0.2	6.1±0.2
Abundance (Solar)	0.31±0.03	0.47±0.05	0.55±0.05	0.55±0.05
Redshift	0.017±0.002	0.017±0.002	0.017±0.002	0.017±0.002
Normalization* (10^{-3} cm $^{-5}$)	11.3±0.2	11.9±0.2	11.2±0.2	11.2±0.3
$\chi^2/\text{d.o.f.}$	379.5/352	378.3/352	378.2/352	378.3/352
Ophiuchus Cluster				
N_{H} (10^{22} cm $^{-2}$)	0.349±0.003	0.519±0.005	0.500±0.004	0.483±0.005
kT_e (keV)	8.08±0.07	8.14±0.08	8.25±0.07	8.28±0.07
Abundance (Solar)	0.427±0.011	0.64±0.02	0.76±0.02	0.76±0.02
Redshift	0.0293±0.0003	0.0293±0.0003	0.0293±0.0003	0.0293±0.0003
Normalization* (10^{-3} cm $^{-5}$)	70.3±0.3	73.7±0.4	69.1±0.3	68.9±0.3
$\chi^2/\text{d.o.f.}$	3551.9/3115	3454.9/3115	3501.0/3115	3518.0/3115
CI 2334+48				
N_{H} (10^{22} cm $^{-2}$)	0.19±0.02	0.25±0.03	0.24±0.03	0.22±0.03
kT_e (keV)	4.1±0.6	4.5±0.5	4.6±0.5	4.6±0.5
Abundance (Solar)	0.44±0.15	0.63±0.21	0.72±0.25	0.72±0.25
Redshift	0.28±0.03	0.29±0.03	0.29±0.02	0.29±0.03
Normalization* (10^{-3} cm $^{-5}$)	1.20±0.10	1.21±0.10	1.14±0.09	1.13±0.13
$\chi^2/\text{d.o.f.}$	235.6/268	237.0/268	238.5/268	238.7/268
CIZA J1358.9–4750 (NW)				
N_{H} (10^{22} cm $^{-2}$)	0.17±0.02	0.24±0.03	0.23±0.03	0.22±0.03
kT_e (keV)	3.6±0.2	3.7±0.2	3.7±0.2	3.7±0.2
Abundance (Solar)	0.26±0.06	0.39±0.09	0.45±0.11	0.45±0.11
Redshift	0.07±0.02	0.07±0.02	0.07±0.02	0.07±0.03
Normalization* (10^{-3} cm $^{-5}$)	4.1±0.3	4.2±0.3	4.0±0.3	4.0±0.3
$\chi^2/\text{d.o.f.}$	158.0/145	153.5/145	156.0/145	155.7/145
CIZA J1358.9–4750 (SE)				
N_{H} (10^{22} cm $^{-2}$)	0.13±0.02	0.19±0.03	0.18±0.03	0.18±0.02
kT_e (keV)	5.6±0.4	5.6±0.4	5.7±0.4	5.7±0.4
Abundance (Solar)	0.45±0.10	0.68±0.11	0.79±0.12	0.79±0.12
Redshift	0.079±0.006	0.079±0.006	0.079±0.009	0.079±0.007
Normalization* (10^{-3} cm $^{-5}$)	4.9±0.2	5.1±0.2	4.8±0.2	4.8±0.2
$\chi^2/\text{d.o.f.}$	220.8/235	224.5/235	223.1/235	223.8/235

Errors are provided at 90% confidence level.

* Defined as $10^{-14} \times \int n_{\text{H}} n_{\text{e}} dV / [4\pi D_{\text{A}}^2 (1+z)^2]$, where n_{H} is the hydrogen density (cm $^{-3}$), n_{e} is the electron density (cm $^{-3}$), D_{A} is the angular distance (cm), z is the redshift, and V is the volume (cm 3).

treated as a free parameter. The slope was derived from the posterior distribution as follows:

$$\text{Model 1 (phabs, angr)} : N_{\text{H}} = (1.01 \pm 0.05) \times 10^{26} \tau_{353} \text{ cm}^{-2} \quad (5)$$

$$\text{Model 2 (phabs, lodd)} : N_{\text{H}} = (1.51 \pm 0.07) \times 10^{26} \tau_{353} \text{ cm}^{-2} \quad (6)$$

$$\text{Model 3 (phabs, wilms)} : N_{\text{H}} = (1.59 \pm 0.10) \times 10^{26} \tau_{353} \text{ cm}^{-2} \quad (7)$$

$$\text{Model 4 (tbabs, wilms)} : N_{\text{H}} = (1.55 \pm 0.10) \times 10^{26} \tau_{353} \text{ cm}^{-2} \quad (8)$$

The errors are statistical errors with a 68% confidence level. The best-fitting model is displayed in each panel.

3.4 Correlation between the N_{H} values and $E(B - V)$

The correlation with between $E(B - V)$ and N_{H} values is well known facts as described in section 1. Thus, we also examined

the relationship between $E(B - V)$ and N_{H} values obtained in the present work. The $E(B - V)$ values were referred to the data by Schlegel et al. (1998)⁴. Figure 3 shows a correlation plot between the $E(B - V)$ and the N_{H} values derived from Model 1–4. As same as the $\tau_{353} - N_{\text{H}}$ relation, we fitted the data with a linear function and obtained the following results.

$$\text{Model 1 (phabs, angr)} : N_{\text{H}} = (6.3 \pm 0.2) \times 10^{21} E(B - V) \text{ cm}^{-2} \quad (9)$$

$$\text{Model 2 (phabs, lodd)} : N_{\text{H}} = (9.4 \pm 0.3) \times 10^{21} E(B - V) \text{ cm}^{-2} \quad (10)$$

$$\text{Model 3 (phabs, wilms)} : N_{\text{H}} = (9.5 \pm 0.3) \times 10^{21} E(B - V) \text{ cm}^{-2} \quad (11)$$

$$\text{Model 4 (tbabs, wilms)} : N_{\text{H}} = (9.3 \pm 0.3) \times 10^{21} E(B - V) \text{ cm}^{-2} \quad (12)$$

The errors are statistical errors with a 68% confidence level. The best-fitting model is displayed in each panel.

⁴ Taken from <https://www.swift.ac.uk/analysis/nhtot/index.php>.

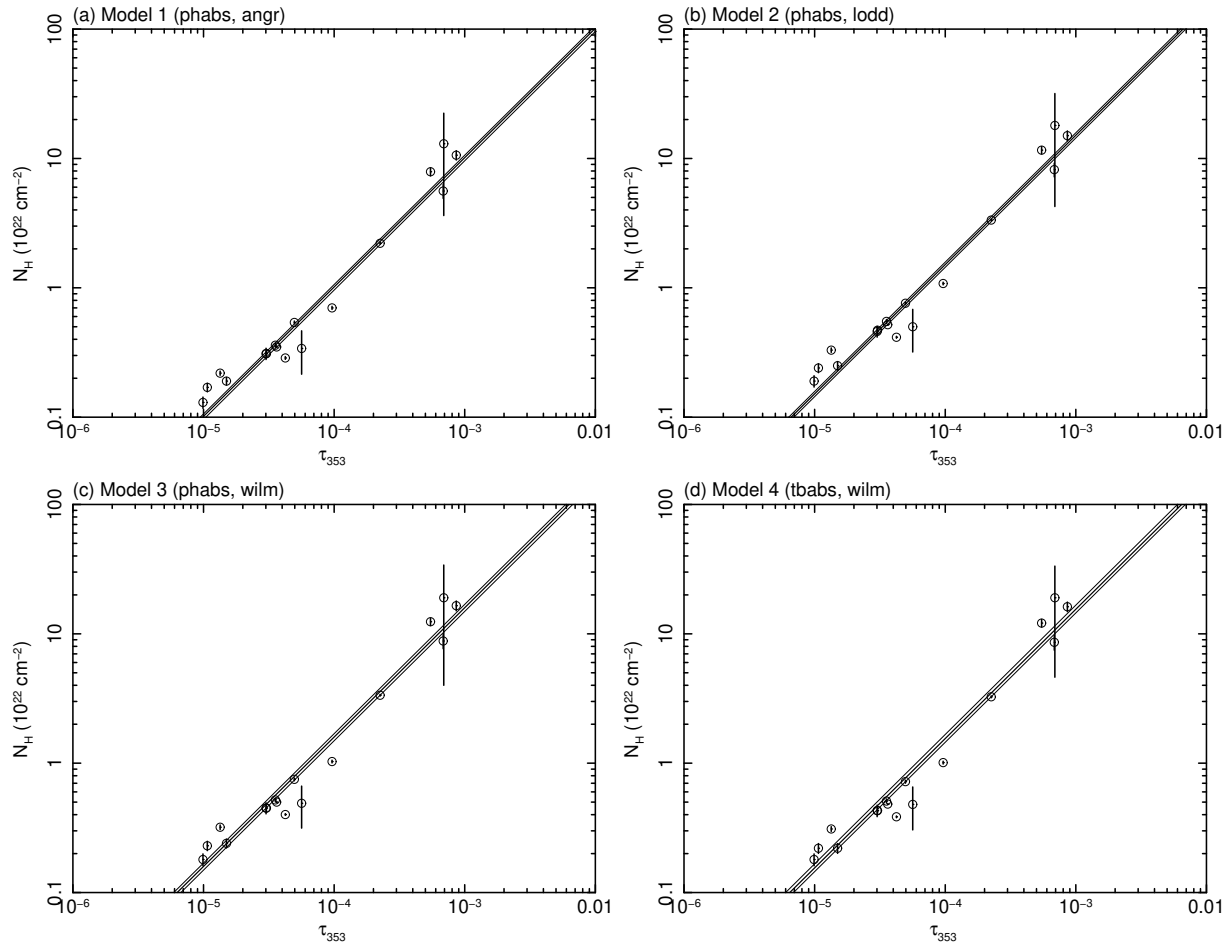


Fig. 2. Correlation plot between the optical depth at 353 GHz, τ_{353} , and the observed N_{H} values, (a) Model 1 (phabs, angr), (b) Model 2 (phabs, lodd), (c) Model 3 (phabs, wilm), and (d) Model 4 (tbabs, wilm). Vertical errors show a 68% confidence level. The thick line shows the best-fitting model (see equation 5–8), whereas the thin lines show the model curve obtained by adding $\pm 1\sigma$ errors of the coefficients of the linear function. Alt text: Line graphs showing the best-fitting results.

4 Discussion and conclusion

We analyzed 17 spectra of 16 clusters of galaxies and the candidates located at the low Galactic latitude using three abundance tables and two photoelectric absorption models, and obtained N_{H} values along the line of sight. We found that the N_{H} values using abundance tables of lodd and wilm are consistent with each other, but the values of angr are about 1.6 times smaller than those of lodd and wilm. This is because that absorption by O is large in the low energy X-rays below 1 keV and the abundance of O relative to H in angr is 1.7 times larger than those in lodd and wilm. On the other hand, differences in the cross sections of photoelectric absorption models of phabs and tbabs are negligible.

We also note that the metal abundances of the X-ray emitting plasma in clusters of galaxies derived using lodd and wilm tables are 1.6–1.7 times larger than that from angr. The metal abundances are estimated from intensities of emission lines in the spectrum. The intensity of the Fe-K line is a good tracer in the plasma with a temperature of ~ 3 –10 keV, thus the difference in the metal abundance in fitting with three abundance tables is because that the abundance of Fe relative to H in angr is larger than those in lodd and wilm.

We found that in all the cases of Model 1–4, the observed N_{H} values are systematically larger than those calculated from equa-

tion (3), in agreement with the fact that a considerable amount of gas is not traced by standard HI or CO line surveys (Grenier et al. 2005). On the other hand, the observed values at high Galactic latitude ($N_{\text{H}} \lesssim 10^{22} \text{ cm}^{-2}$) are comparable to values estimated by equation (4), but the values near to the Galactic plane ($N_{\text{H}} > 10^{22} \text{ cm}^{-2}$) are larger than the estimated values.

Fukui et al. (2014, 2015) pointed out that the relation of the HI integrated intensity and the optical depth at 353 GHz depends on the dust temperature and saturation of the HI emission line at the 21 cm wavelength occurred in the case of low dust temperature. They proposed that optically thick HI would be a likely scenario. Since the values of optical depth of dust at 353 GHz are in the range of 10^{-5} – 10^{-3} , dust radiation is completely transparent through the Galaxy. Fukui et al. (2014) showed a relationship between N_{HI} and τ_{353} of $N_{\text{HI}} = 1.5 \times 10^{26} \tau_{353} \text{ cm}^{-2}$ in the optically thin assumption with a high dust temperature.

The X-ray absorption process is the photoelectric absorption, which depends on the number of atoms to encounter X-ray photons, and hence X-ray observations would be able to derive the N_{H} values independently of the condition of the ISM. Our results show that the obtained N_{H} values in the range of 10^{21} – 10^{23} cm^{-2} are well correlated with the optical depth at 353 GHz, τ_{353} (see figure 2). The dust temperatures of our samples are in the range of

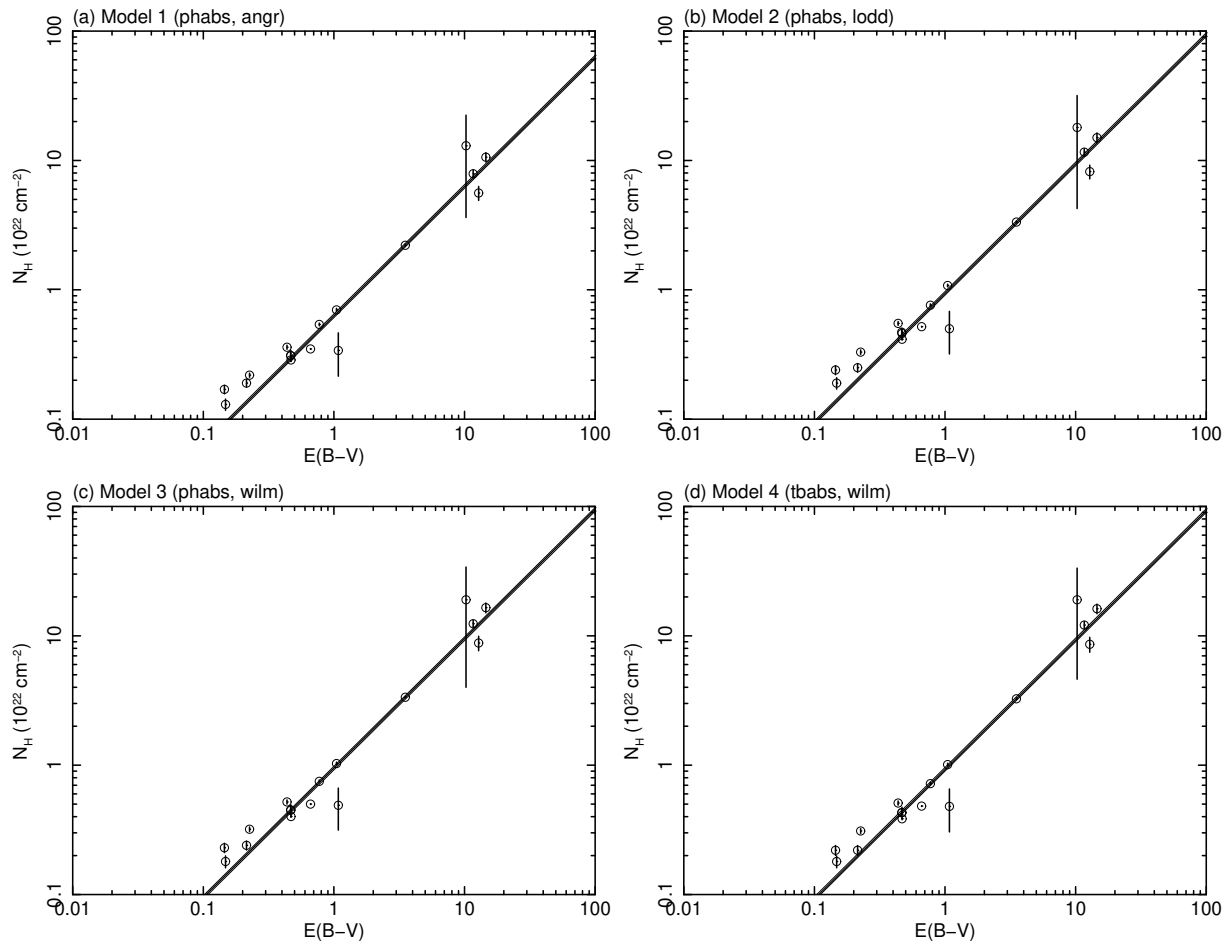


Fig. 3. Correlation plot between the optical reddening, $E(B - V)$, and the observed N_{H} values, (a) Model 1 (phabs, angr), (b) Model 2 (phabs, lodd), (c) Model 3 (phabs, wilm), and (d) Model 4 (tbabs, wilm). Vertical errors show a 68% confidence level. The thick line shows the best-fitting model (see equation 9–12), whereas the thin lines show the model curve obtained by adding $\pm 1\sigma$ errors of the coefficients of the linear function. Alt text: Line graphs showing the best-fitting results.

16.8–22.1 K, but the correlation shows no dependence on the dust temperature. The coefficients depend on the abundance table: the value from *angr* is smaller than those from *wilm* and *lodd*. The relations in the cases of *wilm* and *lodd*, relatively newer abundance tables, are $N_{\text{H}} \sim 1.5 \times 10^{26} \tau_{353} \text{ cm}^{-2}$, which is in agreement with the $N_{\text{H}1-\tau_{353}}$ relation in Fukui et al. (2014).

We also confirmed that $E(B - V)$ and the observed N_{H} values are linearly correlated even at $E(B - V) > 10 \text{ mag}$ and $N_{\text{H}} > 10^{23} \text{ cm}^{-2}$, expressed by $N_{\text{H}} = (6.3 - 9.5) \times 10^{21} E(B - V) \text{ cm}^{-2}$. These are consistent with those obtained in the previous works (Bohlin et al. 1978; Hensley & Draine 2017; Lenz et al. 2017; Li et al. 2018).

In this work, we assumed a single N_{H} value in the spectral analysis for diffuse X-ray emission of clusters of galaxies. Locatelli et al. (2022) states that if the spatial distribution of N_{H} is not considered, X-ray spectral analysis can yield values smaller than the actual N_{H} value and the impact on the value is several times greater, especially when $N_{\text{H}} > 10^{22} \text{ cm}^{-2}$. This would cause deviations from the linear relationships of $\tau_{353} - N_{\text{H}}$ and $E(B - V) - N_{\text{H}}$: the data with the large N_{H} would take values smaller than the linear relationship. The smaller variance of N_{H} value within the source region may give accurate N_{H} estimation. Detailed analysis taking account of the spatial distribution of the ISM column density

within the source region would provide more accurate estimation.

Assuming that the plasma of clusters of galaxies is isothermal, we fitted the spectra of clusters of galaxies with a single temperature component model. Since some clusters of galaxies exhibit temperature distribution, such as cool core and low temperature outskirts, the obtained N_{H} values may have some difference. These may cause the variance around the fitted line. This could be verified by examining the spatial distribution of the plasma temperature within the source region.

Funding

This work was supported by the Japan Society for the Promotion of Science (JSPS) KAKENHI Grant Numbers 21K03615 and 24K00677 (SY, KKN, MN, and HU).

Acknowledgments

This research made use of the NASA/IPAC Extragalactic Database (NED) operated by Jet Propulsion Laboratory, California Institute of Technology, under contract with NASA.

References

- Akamatsu, H., & Kawahara, H. 2013, PASJ, 65, 16
- Anders, E., & Grevesse, N. 1989, *Geochim. Cosmochim. Acta*, 53, 197
- Arnaud, M., & Evrard, A. E. 1999, MNRAS, 305, 631
- Barrière, N. M., Tomsick, J. A., Wik, D. R., Chaty, S., & Roderiguez, J. 2015, ApJ, 799, 24
- Bohlin, R. C., Savage, B. D., & Drake, J. F. 1978, ApJ, 224, 132
- Bolatto, A. D., Wolfire, M., & Leroy, A. K. 2013, ARA&A, 51, 207
- Burke B. E., Mountain R. W., Harrison D. C., Bautz M. W., Doty J. P., Ricker G. R., & Daniels P. J. 1991, IEEE Trans., ED-38, 1069
- Dame, T. M., Hartmann, D., & Thaddeus, P. 2001, ApJ, 547, 792
- Dicky, J. M., & Lockman, F. J. 1990, ARA&A, 28, 215
- Foreman-Mackey, D., Hogg, D. W., Lang, D., Goodman, J. 2013, PASP, 125, 306
- Fukazawa, Y., Makishima, K., & Ohashi, T. 2004, PASJ, 56, 965
- Fukui, Y., et al. 2014, ApJ, 796, 59
- Fukui, Y., Torii, K., Onishi, T., Yamamoto, H., Okamoto, R., Hayakawa, T., Tachihara, K., & Sano, H. 2015, ApJ, 798, 6
- Fujita, Y., et al. 2008, PASJ, 60, 1133
- Gatuzz, E., et al. 2024, A&A, 688, A207
- Gorenstein, P. 1975, ApJ, 198, 95
- Grenier, I. A., Casandjian, J. M., & Terrier, R. 2005, Science, 307, 1292
- Güver, T., & Özel, F. 2009, MNRAS, 400, 2050
- Hensley, B. S., & Draine, B. T. 2017, ApJ, 836, 179
- HI4PI Collaboration 2016, A&A, 594, A116
- Ishisaki, Y., et al. 2007, PASJ, 59, S113
- Kalberla, P. M. W., Burton, W. B., Hartmann, D., Arnal, E. M., Bajaja, E., Morras, R., & Pöppel, W. G. L. 2005, A&A, 440, 775
- Kato, Y., Nakazawa, K., Gu, L., Akahori, T., Takizawa, M., Fujita, Y., & Makishima, K. 2015, PASJ, 67, 71
- Koyama, K., et al. 2007, PASJ, 59, S23
- Kushino, A., Ishisaki, Y., Morita, U., Yamasaki, N. Y., Ishida, M., Ohashi, T., & Ueda, Y. 2002, PASJ, 54, 327
- Lenz, D., Hensley, B. S., & Dor, O. 2017, ApJ, 846, 38
- Li, D., et al. 2018, ApJS, 235, 1
- Locatelli, N., Ponti, G., & Bianchi, S. 2022, A&A, 659, A118
- Lodders, K. 2003, ApJ, 591, 1220
- Lopes de Oliveira, R., Lima Neto, G. B., Mendes de Oliveira, C., Janot-Pacheco, E., & Motch, C. 2006, A&A, 415, 422
- Makishima, K., et al. 1996, PASJ, 48, 171
- Mitsuda, K., et al. 2007, PASJ, 59, S1
- Mori, H., Maeda, Y., Furuzawa, A., Haba, Y., & Ueda, Y. 2013, PASJ, 65, 102
- Mori, H., Maeda, Y., Ueda, Y., Nakazawa, K., & Tawara, Y. 2017, PASJ, 69, 3
- Mullis, C. R., Ebeling, H., Kocevski, D. D., & Tully, R. B. 2005, ASP Conference Series Vol. 329, p183
- Nevalainen, J., Lumb, D., dos Santos, S., Siddiqui, H., Stewart, G., & Parmar, A. N. 2001, A&A, 374, 66
- Nishino, S., Fukazawa, Y., & Hayashi, K. 2012, PASJ, 64, 16
- Nobukawa, K. K., Nobukawa, M., Tsuru, T. G., & Koyama, K. 2015, Adv. in Space Res., 55, 2493
- Ohashi, T., et al. 1996, PASJ, 48, 157
- Planck Collaboration, 2016, A&A, 594, A10
- Planck Collaboration, 2014, A&A, 571, A11
- Planck Collaboration, 2011, A&A, 536, A19
- Predehl, P., & Schmitt, J. H. M. M. 1995, A&A, 293, 889
- Randall, S. W., et al. 2016, ApJ, 823, 94
- Reina, C., & Tarengi, M. 1973, A&A, 26, 257
- Schlegel, D. J., Finkbeiner, D. P., & Davis, M., 1998, ApJ, 500, 525
- Serlemitsos, P. J., et al. 1995, PASJ 47, 105
- Serlemitsos, P., et al. 2007, PASJ, 59, S9
- Smith, D. A., Wilson, A. S., Arnaud, K. A., Terashima, Y., & Young, A. J. 2002, ApJ, 565, 195
- Smith, R. K., Brickhouse, N. S., Liedahl, D. A., & Raymond, J. C. 2001, ApJ, 556, L91
- Smith, R. J., et al. 2014, MNRAS, 441, 1628
- Snowden, S. L., Mushotzky, R. F., Kuntz, K. D., & Davis, D. S. 2008, A&A, 478, 615
- Strüder, L., et al. 2001, A&A, 365, L18
- Sugizaki, M., Mitsuda, K., Kaneda, H., Matsuzaki, K., Yamauchi, S., & Koyama, K. ApJS, 2001, 134, 77
- Taylor, G. B., Govoni, F., Allen, S. W., & Fabian, A. C. 2001, MNRAS, 326, 2
- Turner, M. J. L., et al. 2001, A&A, 365, L27
- Verner, D. A., Ferland, G. J., Korista, K. T., & Yakovlev, D. G. 1996, ApJ, 465, 487
- Wilms, J., Allen, A., & McCray, R. 2000, ApJ, 542, 914
- Willingale, R., et al. 2013, MNRAS, 431, 394
- Wolfire, M. G., Hollenbach, D., & McKee, C. F. 2010, ApJ, 716, 1191
- Yamauchi, S., & Ueno, M. 2025, PASJ, 77, 768
- Yamauchi, S., Ueno, M., Bamba, A., & Koyama, K. 2010, PASJ, 62, 219
- Yamauchi, S., Bamba, A., & Koyama, K. 2011, PASJ, 63, S957